

# Joint multi-band deconvolution for *Euclid* and *Vera C. Rubin* images

U. Akhaury<sup>1</sup>, P. Jablonka<sup>1,2</sup>, F. Courbin<sup>1,3,4</sup>, and J.-L. Starck<sup>5,6</sup>

<sup>1</sup> Laboratory of Astrophysics, Ecole Polytechnique Fédérale de Lausanne (EPFL), Observatoire de Sauverny, CH-1290 Versoix, Switzerland. e-mail: utsav.akhaury@epfl.ch

<sup>2</sup> GEPI, Observatoire de Paris, Université PSL, CNRS, 5 Place Jules Janssen, 92190 Meudon, France.

<sup>3</sup> ICC-UB Institut de Ciències del Cosmos, Universitat de Barcelona, Martí Franquès, 1, E-08028 Barcelona, Spain.

<sup>4</sup> ICREA, Pg. Lluís Companys 23, Barcelona, E-08010, Spain.

<sup>5</sup> Université Paris-Saclay, Université Paris Cité, CEA, CNRS, AIM, 91191, Gif-sur-Yvette, France

<sup>6</sup> Institutes of Computer Science and Astrophysics, Foundation for Research and Technology Hellas (FORTH), Greece

Received September 15, 1996; accepted March 16, 1997

## ABSTRACT

With the advent of surveys like *Euclid* and *Vera C. Rubin*, astrophysicists will have access to both deep, high-resolution images, and multi-band images. However, these two conditions are not simultaneously available in any single dataset. It is therefore vital to devise image deconvolution algorithms that exploit the best of the two worlds and that can jointly analyze datasets spanning a range of resolutions and wavelengths. In this work, we introduce a novel multi-band deconvolution technique aimed at improving the resolution of ground-based astronomical images by leveraging higher-resolution space-based observations. The method capitalizes on the fortunate fact that the *Vera C. Rubin* *r*-, *i*-, and *z*-bands lie within the *Euclid* *VIS* band. The algorithm jointly deconvolves all the data to turn the *r*-, *i*-, and *z*-band *Vera C. Rubin* images to the resolution of *Euclid* by enabling us to leverage the correlations between the different bands. We also investigate the performance of deep learning-based denoising with DRUNet to further improve the results. We illustrate the effectiveness of our method in terms of resolution and morphology recovery, flux preservation, and generalization to different noise levels. This approach extends beyond the specific *Euclid-Rubin* combination, offering a versatile solution to improve the resolution of ground-based images in multiple photometric bands by jointly using any space-based images with overlapping filters.

**Key words.** Deconvolution – *Euclid* – *Vera C. Rubin* – HST

## 1. Introduction

High spatial resolution, high signal-to-noise ratio, and broad wavelength coverage are all essential to most observational challenges in astrophysics. However, it is difficult, or even impossible, to make these three miracles happen simultaneously. Space telescopes, although free of atmospheric turbulence, are limited in size. Ground-based telescopes can deliver high signal-to-noise data but are affected by atmospheric turbulence and have a higher sky background. In addition, blurring by the instrumental or atmospheric Point Spread Function (PSF) differs in each type of data and varies from band to band. To capitalise on the strengths of all types of telescopes and data, it is crucial to develop robust deconvolution techniques that can remove blurring by the PSF and that can optimize the signal-to-noise ratio of the final reconstruction, by combining all observations accounting for the different bands and PSFs.

Due to the presence of noise, image deconvolution is a challenging ill-posed inverse problem that requires regularization for a well-defined solution. Early approaches in the field acknowledged this issue, proposing solutions such as minimising the Tikhonov function (Tikhonov & Arsenin 1977) or maximising the entropy of the solution (Skilling & Bryan 1984). Bayesian methods also emerged, including the Richardson-Lucy algorithm applied to early *Hubble* Space Telescope (HST) data (Richardson 1972; Lucy 1974). A novel approach proposed by Magain et al. (MCS; 1998) separated point sources from extended ones and used a narrow PSF for deconvolution to achieve an improved

resolution suitable for the chosen pixel sampling. This approach was enhanced with wavelet regularization for the extended channel (Cantale et al. 2016), and further refined by Michalewicz et al. (STARRED; 2023), who employed Starlets, an isotropic wavelet basis (Starck et al. 2015), to regularize the solution. There have also been efforts to jointly deconvolve multiple astronomical observations of the same sky region (Donath et al. 2023). Furthermore, Ingaramo et al. (2014) explored the combination of multiple sources by demonstrating the application of Richardson-Lucy deconvolution to merge high-resolution, high-noise images with low-resolution, low-noise images.

A notable advancement in astronomical deconvolution was the use of deep learning. Once trained, deep learning-based methods also offer significant computational efficiency compared to traditional approaches. U-Nets (Ronneberger et al. 2015) have gained popularity for their nonlinear processing capabilities and multi-scale architecture. Expanding on U-Nets, Sureau et al. (2020) introduced the Tikhonet method for deconvolving optical galaxy images, demonstrating superior performance over sparse regularization methods in terms of mean squared error (MSE) and a shape criterion that assesses galaxy ellipticity. Nammour et al. (2022) enhanced Tikhonet by incorporating a shape constraint into the loss function, achieving further improvements. Another powerful architecture, Learnlet (Ramzi et al. 2023), combines the strengths of wavelets and U-Nets while offering a fully interpretable neural network with minimal hallucination. In our previous work (Akhaury et al. 2022, 2024), we proposed a two-step deconvolution framework and investigated the performance

of CNN and transformer-based denoisers. We concluded that a Swin transformer-based U-Net (SUNet, Fan et al. (2022)) outperformed a CNN-based U-Net (Ronneberger et al. 2015) in terms of normalised mean squared error (NMSE) and structural similarity index measure (SSIM).

While deconvolution is primarily used to reconstruct galaxy images at high spatial resolution in each photometric band independently, there are scenarios, particularly at low signal-to-noise ratios, where joint multi-band deconvolution can enhance the detection and characterization of systems. One such potential application is the joint multi-band deconvolution of *Euclid* and *Vera C. Rubin* images. The *Vera C. Rubin* Observatory is set to deliver a dataset of 500 petabytes across multiple optical frequency bands, while *Euclid* will observe images spanning the optical and infrared spectrum. Interestingly, the *Euclid* VIS-band (central frequency = 715 nm) overlaps with three of the *Vera C. Rubin* filters: *r*, *i*, *z*. As a space-based satellite, *Euclid* will produce images with sharper details due to its narrower PSF compared to *Vera C. Rubin*. A related study by Joseph et al. (2021) also involves jointly modelling simulated images that model observations from both *Euclid* and *Vera C. Rubin*.

In this work, we present a novel multi-band deconvolution technique designed to enhance the resolution of ground-based astronomical images by leveraging higher-resolution space-based observations. Our approach, which focusses on the joint deconvolution of *Vera C. Rubin* and *Euclid* images, effectively exploits the overlapping spectral coverage of the *Rubin* *r*-, *i*-, and *z*-bands with the *Euclid* VIS-band. By utilizing the *Euclid* VIS-band image as a term that provides additional information, our technique ensures that the deconvolved *Rubin* images retain high spatial resolution and accurate photometric measurements. The integration of deep learning-based denoising further enhances the quality of the deconvolved outputs, reducing background noise without altering the main structures of the galaxies. We generate the realistic *Euclid* and *Vera C. Rubin* simulations from HST cutouts of varying magnitudes extracted from the GOODS-N and GOODS-S surveys (Retzlaff, J. et al. 2010). The simulated *Euclid*-like VIS-band PSF was obtained from Liaudat et al. (2022), and the simulated *Rubin*-like *r*-, *i*-, and *z*-band PSFs were obtained from Abolfathi et al. (2021). Our method demonstrates effectiveness in terms of resolution recovery, flux preservation, and generalization across different noise levels. Through our joint deconvolution approach, we achieve resolution recovery in *Vera C. Rubin* simulated images close to that of HST, a feat nearly impossible with independent deconvolution of each photometric band. The potential applications of our method go beyond the *Euclid*-*Rubin* pair, providing a flexible solution to enhance the resolution of ground-based images in multiple photometric bands with any overlapping space-based filter band. This versatility is especially important as large-scale astronomical surveys gather increasing amounts of data, creating a need for effective and reliable deconvolution techniques.

In Section 2, we describe the deconvolution problem and introduce our proposed solution. The methodology for generating our dataset is detailed in Section 3. We then present the outcomes of our deconvolution algorithm in Section 4. Finally, Section 5 presents our conclusions. To support reproducible research, the codes utilised in this article are publicly accessible in Section 6.

## 2. The deconvolution problem

### 2.1. The forward model

For the three *Vera C. Rubin* filters, let  $\mathbf{y}_r, \mathbf{y}_i, \mathbf{y}_z \in \mathbb{R}^{n \times n}$  be the corresponding observed images and  $\mathbf{h}_r, \mathbf{h}_i, \mathbf{h}_z \in \mathbb{R}^{n \times n}$  be the PSFs. If  $\mathbf{x}_r^t, \mathbf{x}_i^t, \mathbf{x}_z^t \in \mathbb{R}^{n \times n}$  denote the corresponding target images,  $*$  denotes the convolution operation, and  $\eta_r, \eta_i, \eta_z \in \mathbb{R}^{n \times n}$  denote additive noise, the observed *Rubin* images can then be modelled as:

$$\mathbf{y}_r = \mathbf{h}_r * \mathbf{x}_r^t + \eta_r \quad (1)$$

$$\mathbf{y}_i = \mathbf{h}_i * \mathbf{x}_i^t + \eta_i \quad (2)$$

$$\mathbf{y}_z = \mathbf{h}_z * \mathbf{x}_z^t + \eta_z \quad (3)$$

As for *Euclid*, let  $\mathbf{y}_{euc} \in \mathbb{R}^{n \times n}$  be the observed image,  $\mathbf{x}_{euc}^t \in \mathbb{R}^{n \times n}$  be the target image, and  $\mathbf{h}_{euc} \in \mathbb{R}^{n \times n}$  be the PSF. If  $\eta_{euc} \in \mathbb{R}^{n \times n}$  denotes additive noise and  $\alpha_r, \alpha_i, \alpha_z \in \mathbb{R}^n$  denote the corresponding fractional flux contribution from each *Vera C. Rubin* filter, the target and the observed images can be modelled as:

$$\mathbf{x}_{euc}^t = \alpha_r \mathbf{x}_r^t + \alpha_i \mathbf{x}_i^t + \alpha_z \mathbf{x}_z^t \quad (4)$$

$$\mathbf{y}_{euc} = \mathbf{h}_{euc} * \mathbf{x}_{euc}^t + \eta_{euc} \quad (5)$$

The motivation behind taking the weighted sum of the *Vera C. Rubin* images to model the *Euclid* image can be seen in Figure 1, which shows the overlap between the *Rubin* and *Euclid* filters.

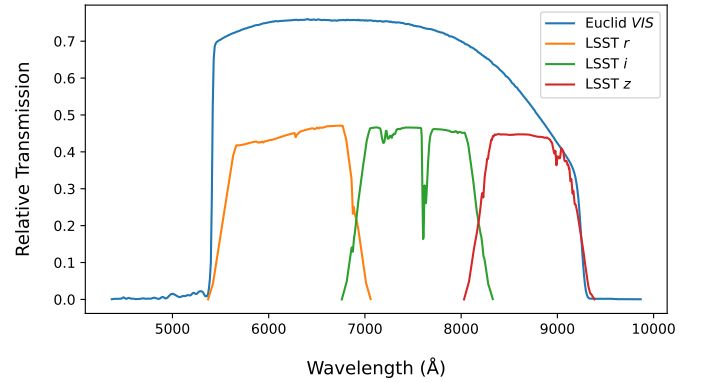


Fig. 1: The filter curves for *Euclid* and *Vera C. Rubin*, which display the relative filter transmission as a function of the wavelength. The *Euclid* VIS-band overlaps with three of the *Vera C. Rubin* filters: *r*, *i*, *z*.

### 2.2. The proposed solution

We formulated the following loss functions and minimize them using gradient descent to recover the optimal solutions:

$$L_r(\mathbf{x}_r) = \frac{1}{2} \left\| \frac{\mathbf{h}_r * \mathbf{x}_r - \mathbf{y}_r}{\sigma_r} \right\|_F^2 + \lambda_r \mathbf{K} \quad (6)$$

$$L_i(\mathbf{x}_i) = \frac{1}{2} \left\| \frac{\mathbf{h}_i * \mathbf{x}_i - \mathbf{y}_i}{\sigma_i} \right\|_F^2 + \lambda_i \mathbf{K} \quad (7)$$

$$L_z(\mathbf{x}_z) = \frac{1}{2} \left\| \frac{\mathbf{h}_z * \mathbf{x}_z - \mathbf{y}_z}{\sigma_z} \right\|_F^2 + \lambda_z \mathbf{K} \quad (8)$$

$$\text{where } \mathbf{K} = \left\| \frac{\mathbf{h}_{euc} * \sum_{c \in \{r,i,z\}} \alpha_c \mathbf{x}_c - \mathbf{y}_{euc}}{\sigma_{euc}} \right\|_F^2 \quad (9)$$

The first terms in equations 6-8 represent the data fidelity terms for each respective band, with  $\sigma_r$ ,  $\sigma_i$ ,  $\sigma_z$  being the corresponding noisemaps. The second terms are the constraining terms that enforce the condition that the sum of images in the *Rubin*  $r$ -,  $i$ -, and  $z$ -band images equals the *Euclid*  $VIS$ -band images, as expected from Figure 1 after flux calibration. Within these constraining terms, the individual images  $x_r$ ,  $x_i$ , and  $x_z$  are multiplied by their respective fractional flux contributions  $\alpha_r$ ,  $\alpha_i$ , and  $\alpha_z$ , which represent the fractional area overlaps between their corresponding filter curves. The values of  $\alpha_r$ ,  $\alpha_i$ , and  $\alpha_z$  are obtained by integrating the area under the curves in Figure 1 and normalising them to sum up to one. The resulting values are  $\alpha_r = 0.3785$ ,  $\alpha_i = 0.3468$ , and  $\alpha_z = 0.2746$ . The denominator,  $\sigma_{euc}$ , denotes the *Euclid* image noisemap. The choice of the multiplicative hyperparameters  $\lambda_r$ ,  $\lambda_i$ , and  $\lambda_z$  is described in Section 2.3.

### 2.3. Hyper-parameter tuning

The hyper-parameters  $\lambda_r$ ,  $\lambda_i$ , and  $\lambda_z$  are determined by varying the ratios between the second and first terms in equations 6-8. These ratios indicate the contribution coming from the constraining term. We varied the ratios from 0 (no contribution from the constraining term) to 1 (equal contribution from the constraining term) in steps of 0.01. From this experiment, the optimal solution yields the lowest MSE with a ratio of 0.3 for all three photometric bands. Subsequently, the values of  $\lambda_r$ ,  $\lambda_i$ , and  $\lambda_z$  are computed from these ratios by dividing them by  $\mathbf{K}$  (equation 9).

### 2.4. Optimization

The aim is to find optimal solutions  $\hat{\mathbf{x}}_r$ ,  $\hat{\mathbf{x}}_i$ ,  $\hat{\mathbf{x}}_z$  that minimise the individual loss functions:

$$\hat{\mathbf{x}}_{\{r,i,z\}} = \underset{\mathbf{x}_{\{r,i,z\}}}{\operatorname{argmin}} L_{\{r,i,z\}}(\mathbf{x}_{\{r,i,z\}})$$

which is done in an alternative and iterative manner using gradient descent:

$$\mathbf{x}_{\{r,i,z\}}^{[k+1]} = \mathbf{x}_{\{r,i,z\}}^{[k]} - \beta_{\{r,i,z\}} \nabla L_{\{r,i,z\}}(\mathbf{x}_{\{r,i,z\}}^{[k]}) \quad (10)$$

where  $\mathbf{x}^{[k]}$  denotes the variable  $\mathbf{x}$  at  $k^{\text{th}}$  iteration, and  $\beta_r, \beta_i, \beta_z \in \mathbb{R}^n$  are the step-sizes chosen such that convergence is guaranteed (described in more detail in Section 2.5). While computing equation 10 for one band, it is assumed that the other two bands are known and remain constant. The gradients of the loss functions 6-8 are given by:

$$\nabla L_r(\mathbf{x}_r) = \frac{\mathbf{h}_r^\top * (\mathbf{h}_r * \mathbf{x}_r - \mathbf{y}_r)}{\|\sigma_r\|_F^2} + \lambda_r \alpha_r \mathbf{K}_{grad} \quad (11)$$

$$\nabla L_i(\mathbf{x}_i) = \frac{\mathbf{h}_i^\top * (\mathbf{h}_i * \mathbf{x}_i - \mathbf{y}_i)}{\|\sigma_i\|_F^2} + \lambda_i \alpha_i \mathbf{K}_{grad} \quad (12)$$

$$\nabla L_z(\mathbf{x}_z) = \frac{\mathbf{h}_z^\top * (\mathbf{h}_z * \mathbf{x}_z - \mathbf{y}_z)}{\|\sigma_z\|_F^2} + \lambda_z \alpha_z \mathbf{K}_{grad} \quad (13)$$

$$\text{where } \mathbf{K}_{grad} = \frac{2\mathbf{h}_{euc}^\top}{\|\sigma_{euc}\|_F^2} * \left( \mathbf{h}_{euc} * \sum_{c \in \{r,i,z\}} \alpha_c \mathbf{x}_c - \mathbf{y}_{euc} \right) \quad (14)$$

### 2.5. Gradient descent step-size

Suppose a function  $f: \mathbb{R}^{n \times n} \rightarrow \mathbb{R}^{n \times n}$  which is convex and differentiable. Its gradient is Lipschitz continuous if there exists some constant  $C$  such that:

$$\|\nabla f(\mathbf{x}') - \nabla f(\mathbf{x})\| \leq C \|\mathbf{x}' - \mathbf{x}\|$$

Since the loss functions 6-8 are convex and differentiable, one could find Lipschitz constants  $C_{\{r,i,z\}}$  such that:

$$\begin{aligned} \|\nabla L_{\{r,i,z\}}(\mathbf{x}'_{\{r,i,z\}}) - \nabla L_{\{r,i,z\}}(\mathbf{x}_{\{r,i,z\}})\| &\leq C_{\{r,i,z\}} \|\mathbf{x}'_{\{r,i,z\}} - \mathbf{x}_{\{r,i,z\}}\| \\ C_{\{r,i,z\}} &\geq \frac{\mathbf{h}_{\{r,i,z\}}^\top * \mathbf{h}_{\{r,i,z\}}}{\|\sigma_{\{r,i,z\}}\|_F^2} + 2\lambda_{\{r,i,z\}} \alpha_{\{r,i,z\}}^2 \mathbf{h}_{euc}^\top * \mathbf{h}_{euc} \end{aligned} \quad (15)$$

Once that is found, the optimal constraints on the individual step-sizes  $\beta_{\{r,i,z\}}$  that ensure convergence are as follows:

$$\beta_{\{r,i,z\}} \leq \frac{1}{C_{\{r,i,z\}}} \quad (16)$$

From equations 15 and 16, it is important to note that the step-size also depends on the *Rubin* and *Euclid* PSFs (detailed in Sections 3.2 and 3.3), the values of  $\lambda_{\{r,i,z\}}$  (described in Section 2.3) and  $\alpha_{\{r,i,z\}}$  (shown in Section 2.2).

## 3. Dataset generation

### 3.1. Ground truth images

We extracted HST cutout windows of dimensions  $128 \times 128$  pixels from GOODS-N and GOODS-S (Retzlaff, J. et al. 2010) in the  $F606W$ ,  $F775W$ , and  $F850LP$  bands by centering them at the centroid of the object. These HST bands were selected because their central wavelengths align with those of the *Rubin*  $r$ -,  $i$ -, and  $z$ -bands, and these HST images were subsequently used to simulate the *Rubin* images, as explained in Section 3.2. The mosaiced HST ACS images along with the catalogue can be found at this link<sup>1</sup>. These HST cutouts are at a pixel scale of  $0.05''$ . We aimed to perform the experiments on galaxies with sizes large enough to effectively assess the impact of deconvolution on our ability to resolve their structural and morphological features, such as arms, bars, and clumps. To ensure the selection of large galaxies and exclude point-sized objects, we applied the following filtering criteria to the  $F775W$  band catalogue:

- $18 < \text{MAG\_AUTO} < 23$  (AB magnitude in SExtractor “AUTO” aperture)
- $\text{Flux\_Radius}_{80} > 10$  (80% enclosed flux radius in pixels)
- $\text{FWHM} > 10$  (full width at half maximum in pixels)

We then visually inspected and selected 92 objects that exhibited extended and complex galaxy structures. The histogram of the HST  $F775W$  band magnitude for all galaxies in our dataset is shown in Figure 2. It is important to highlight that according to our simulations, the HST  $F775W$  band corresponds to the *Rubin*  $i$ -band, and we will refer to it as the *Rubin*  $i$ -band throughout the text.

<sup>1</sup> <https://archive.stsci.edu/prepds/goods/>

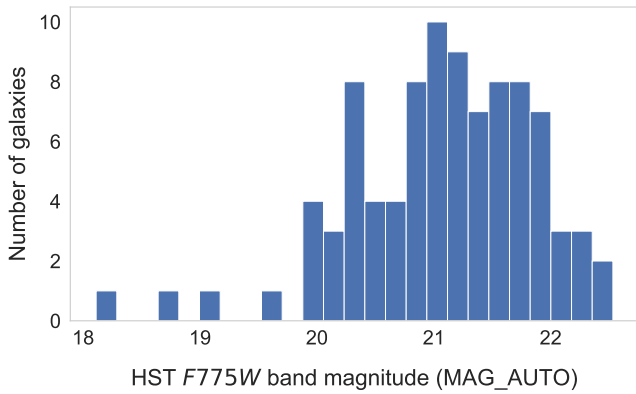


Fig. 2: Histogram of the HST *F775W* band magnitude for all galaxies in our dataset after filtering. Note that the HST *F775W* band matches with the *Rubin i*-band.

### 3.2. Vera C. Rubin images

The simulated *Vera C. Rubin*-like PSFs were obtained from the second data challenge (DC2) of the Legacy Survey of Space and Time (LSST) Dark Energy Science Collaboration (DESC). The atmospheric and optical effects, as well as sensor-induced electrostatic effects, are simulated using physically motivated models, with a final adjustment to the PSF sizes to match the expected data from the Rubin Observatory, as described in detail in Abolfathi et al. (2021).

To generate the *Vera C. Rubin* simulated images, we first convolved the HST images in the *F606W*, *F775W*, and *F850LP* bands with the *Rubin r*-, *i*-, and *z*-band PSFs, respectively, such that the simulated images are at the expected *Rubin* resolution, with a pixel scale of  $0.2''$ . Subsequently, we added white Gaussian noise such that our *Rubin*-simulated images have a signal-to-noise (S/N) ratio ranging between 12 and 28, with a median around 20. Based on the survey parameters outlined in Željko Ivezić et al. (2019), our simulations suggest an S/N range that corresponds to the initial few visits of the telescope. This indicates that our method could be effectively applied as soon as the first images start arriving.

### 3.3. Euclid images

The simulated *Euclid*-like *VIS*-band PSF was obtained using the WaveDiff model proposed by Liaudat et al. (2022), which changes the data-driven PSF modelling space from the pixels to the wavefront by adding a differentiable optical forward model in the modelling framework. WaveDiff outputs an approximation of the true *Euclid* PSF, which was derived before the actual launch of the satellite.

Next, we calculated the fractional flux contributions  $\alpha_r, \alpha_i, \alpha_z$  by integrating the area under the curves in Figure 1 and normalising them to sum to 1. The resulting values, as also mentioned in Section 2.2, are  $\alpha_r = 0.3785$ ,  $\alpha_i = 0.3468$ , and  $\alpha_z = 0.2746$ . To generate the *Euclid* simulated images, we multiplied  $\alpha_r, \alpha_i, \alpha_z$  with the HST images in the *F606W*, *F775W*, and *F850LP* bands, respectively. The result is then convolved with the simulated *Euclid* PSF, such that the simulated images are at the expected *Euclid* resolution with a pixel scale of  $0.1''$ . Finally, white Gaussian noise is added such that the *Euclid*-simulated images have a signal-to-noise (S/N) ratio ranging between 20 and 45, with a median around 35. Based on the calculations presented by Euclid Collaboration et al. (2022) which assess the S/N statistics for Eu-

clid, our simulations are conservative, implying that our method would perform well when applied to real images with higher S/N.

## 4. Results

The algorithm simultaneously processed the noisy simulations from the three *Vera C. Rubin* bands and the *Euclid VIS*-band, along with their respective PSFs. These noisy images served as initializations or first guesses for the algorithm. Subsequently, the algorithm iteratively minimised the loss functions 6-8, as detailed in Section 2.4. The algorithm was run for 200 iterations, with convergence typically observed within 50-100 iterations for all images in our dataset. Figure 3 shows the convergence plot of the loss function for the deconvolved output in Figure 7a.

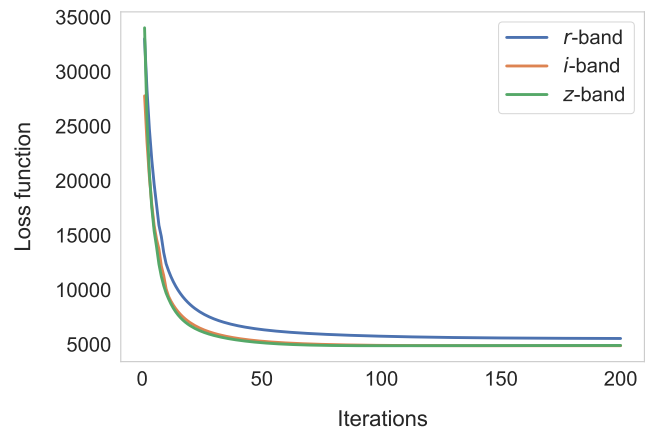


Fig. 3: The loss function for the galaxy shown in Figure 7a. Convergence is guaranteed at around 100 iterations when the relative change in loss value  $< 10^{-3}$  and the curve is flat.

### 4.1. Flux leakage test

As a validation to ensure no flux leakage between channels during the joint deconvolution of *Vera C. Rubin* and *Euclid* images, we conducted a unit test. We assumed three distinct Gaussians placed separately in the *Rubin* channels, with the *Euclid* simulation being a weighted sum of these three images, resulting in three disjoint Gaussians. Post-deconvolution, the Gaussians remained intact without any structure extending beyond their boundaries. This confirms that the structure present in the deconvolved image within each *Rubin* band is independent of the structures in other bands and each image accurately retains only the information relevant to its specific band. Figure 4 provides a visual demonstration of these findings.

Moreover, to further validate that our method is effective for objects with non-flat spectral energy distributions (SEDs), we analyzed the transfer of information across different bands for such objects. The results are presented in Appendix A.

### 4.2. Deconvolved outputs

We present two examples of deconvolved images in Figure 7, illustrating the algorithm's capability to recover features that were lost in the original *Vera C. Rubin* simulations. Visually, the deconvolved outputs seem to capture the variations between different bands. Qualitatively, these outputs exhibit high quality with minimal background noise and result in clean residuals. However,

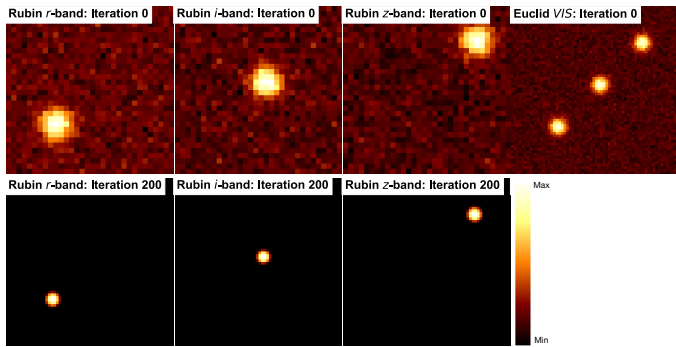


Fig. 4: Unit test to verify that there is no leakage of flux from one channel to another. The recovered Gaussians remain at their original centers.

in the next Section, 4.3, we demonstrate that employing a deep learning-based denoiser further enhances the already impressive results achieved initially. Table 1 presents the normalized mean squared error (NMSE) computed with respect to the ground-truth HST image for the pre-denoised and post-denoised images.

#### 4.3. Deep learning-based denoising

After obtaining the deconvolved outputs, we feed them to DRUNet, a neural network proposed by Zhang et al. (2022) that combines U-Net (Ronneberger et al. 2015) and ResNet (He et al. 2016). U-Net is renowned for its efficiency in image-to-image translation, while ResNet excels in increasing modelling capacity through stacked residual blocks. Inspired by FFDNet (Zhang et al. 2018a), which incorporates a noise level map as input, DRUNet enhances U-Net by integrating residual blocks to improve prior denoising modelling. Similar approaches that combine U-Net and ResNet can be found in other studies (Zhang et al. 2018b; VenkateshG et al. 2018). The backbone of DRUNet is a U-Net architecture with four scales, and the schematic proposed by Zhang et al. (2022) is depicted in Figure 5.

We chose DRUNet because it is a non-blind denoiser, meaning it takes the noise map as input. This ensures that any unknown noise can be estimated and given as input for denoising. We estimate the noise level map in our deconvolved images using the scikit-image package (van der Walt et al. 2014) by calculating the average noise level within four  $16 \times 16$  pixel squares placed at each corner of the image. This approach ensures that only background noise is measured, avoiding any contribution from the signal. This map is then fed to the pre-trained DRUNet, along with the deconvolved image. The denoised outputs are illustrated in Figure 8. It is observed that the denoiser exclusively eliminates noise from the background without affecting the main structure of the galaxies. Although the enhancement in image quality is marginal (since the original deconvolved image is already of high quality), the normalized mean squared error (NMSE) computed with respect to the ground-truth HST image decreases, as shown in Table 1. The most notable improvement is observed in the  $z$ -band images. Even though DRUNet was trained on a combination of images from BSD (Chen & Pock 2017), Waterloo Exploration Database (Ma et al. 2017), DIV2K (Agustsson & Timofte 2017), and Flickr2K (Lim et al. 2017), it is remarkable that it works well on astronomical data, showing great generalization. Finally, the fractional error in the output flux as a function of the  $i$ -band magnitude is shown in Figure 6, which indicates that the mean

flux error is less than 5% for the entire magnitude range for all the bands.

Table 1: NMSE with respect to HST images.

| NMSE           | $r$ -band | $i$ -band | $z$ -band |
|----------------|-----------|-----------|-----------|
| Pre-denoising  | 0.059     | 0.041     | 0.053     |
| Post-denoising | 0.058     | 0.038     | 0.038     |
| % improvement  | 1.69%     | 7.32%     | 28.3%     |

**Notes.** NMSE is calculated for the pre-denoised and post-denoised images with respect to the ground-truth HST image.

#### 4.4. Improvement compared to independent deconvolution of each band

To demonstrate the advantages of jointly deconvolving multiple photometric bands, we performed independent deconvolution of each band using the deconvolution framework introduced in Akhaury et al. (2024). The method proceeds in two steps: it first deconvolves the input using Tikhonov regularization (Tikhonov & Arsenin 1977), and denoises the result using SUNet (Fan et al. 2022), a state-of-the-art Swin transformer-based architecture. The results, presented in Figure 9, show that the joint deconvolution method outperforms the independent deconvolution of individual bands. The joint method enables us to leverage the correlation between the different bands and the space-based image, thus improving the final output.

## 5. Conclusion

In this work, we have presented a novel image deconvolution technique designed to improve the resolution of multi-band ground-based data by leveraging higher-resolution space-based observations. Our approach, which focusses on the joint deconvolution of *Vera C. Rubin* and *Euclid* images, effectively exploits the overlapping spectral coverage of the *Rubin*  $r$ -,  $i$ -, and  $z$ -bands with the *Euclid VIS*-band. Through rigorous testing, we demonstrated that our iterative algorithm successfully recovers fine details while preserving the flux for each band. Different noise levels were tested, and the resolution achieved by ground-based data is close to that of HST. Our results indicate that joint deconvolution of all data outperforms independent deconvolution of individual photometric bands using existing state-of-the-art methods. By utilising the *Euclid VIS*-band image as a term that provides additional information, our technique ensures that the deconvolved *Rubin* images retain high spatial resolution and accurate photometric measurements. The integration of deep learning-based denoising using DRUNet enhances the quality of the deconvolved output, further reducing background noise without altering the main structures of the galaxies.

The potential applications of our method extend beyond the *Euclid-Rubin* pair, offering a versatile solution to improve the resolution of ground-based images in multiple photometric bands as long as there exists a space-based image of the same field of view in a band that encompasses all ground-based filters. In the future, we intend to test our deconvolution method on images of the Perseus cluster by using ground-based observations from the *CFHT* (*Canada–France–Hawaii Telescope*) and space-based observations from the *Euclid ERO* (*Early Release Observations*) public release.

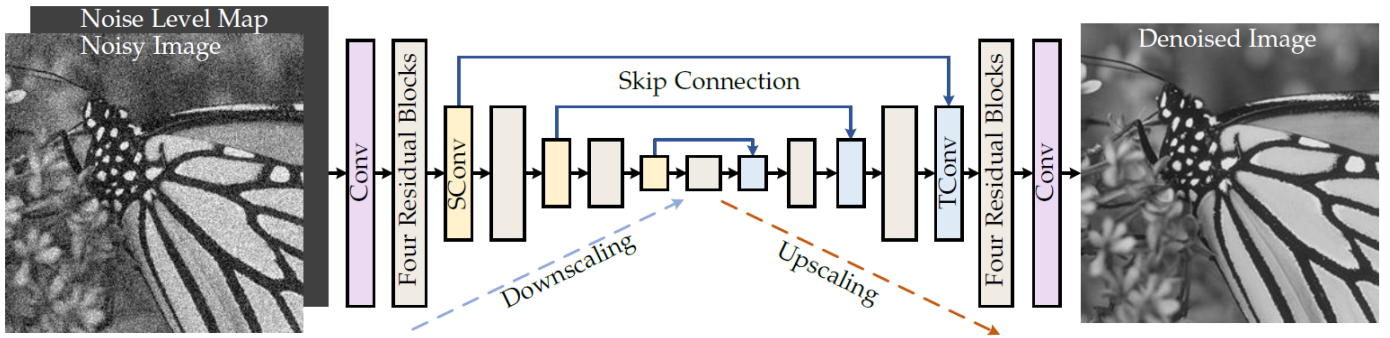


Fig. 5: The DRUNet architecture, which incorporates an additional noise level map as input and integrates U-Net (Ronneberger et al. 2015) with ResNet (He et al. 2016). "SConv" stands for strided convolution and "TConv" stands for transposed convolution. Image credits: Zhang et al. (2022).

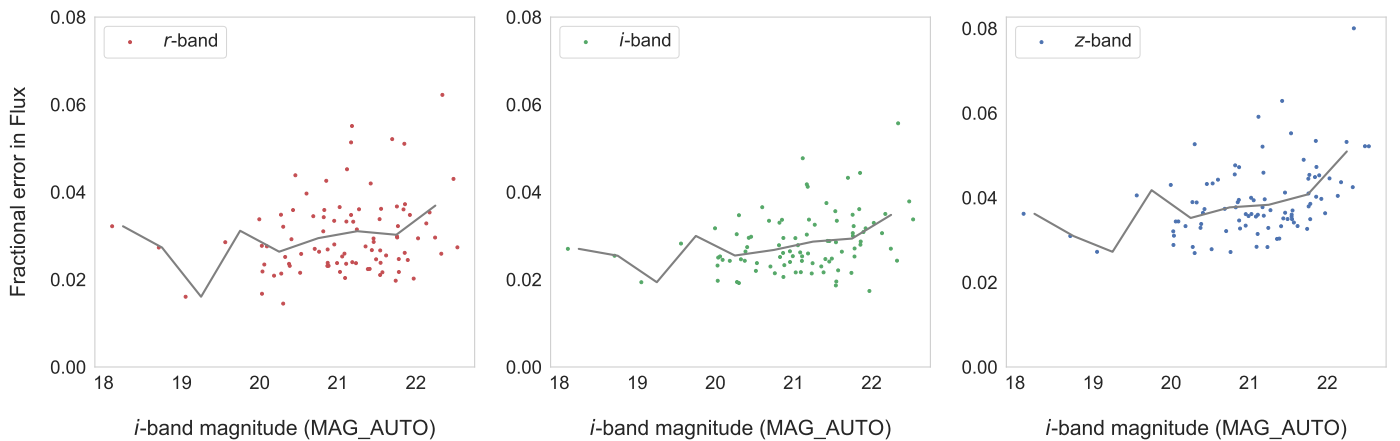


Fig. 6: Fractional error in the output flux as a function of the *i*-band magnitude (which is chosen in order to have the same scale on the x-axes). The dots correspond to the individual galaxies, and the grey line is the best-fit line after binning the magnitude values.

## 6. Data availability

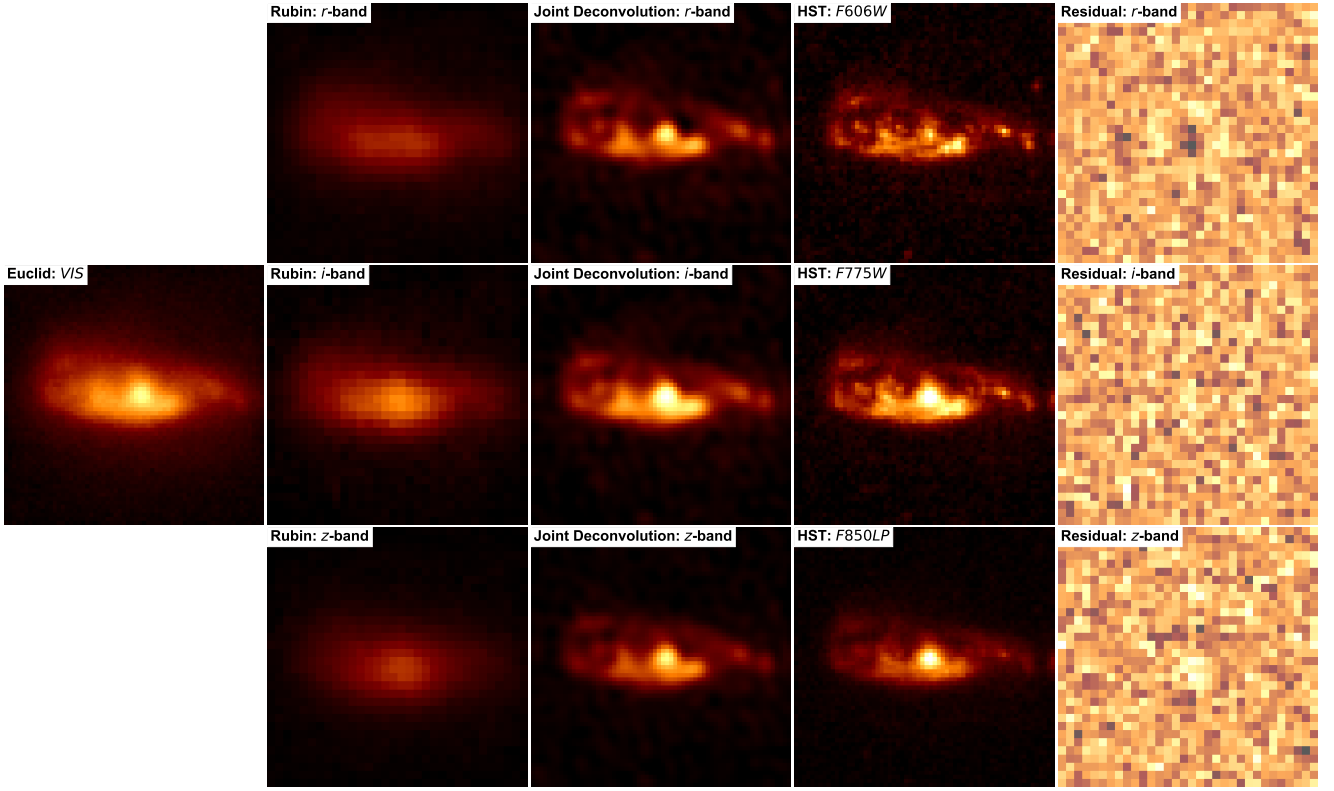
For the sake of reproducible research, the codes used for this article are publicly available online.

1. The ready-to-use version of our joint deconvolution method<sup>2</sup>.
2. The DRUNet repository from Zhang et al. (2022)<sup>3</sup>.

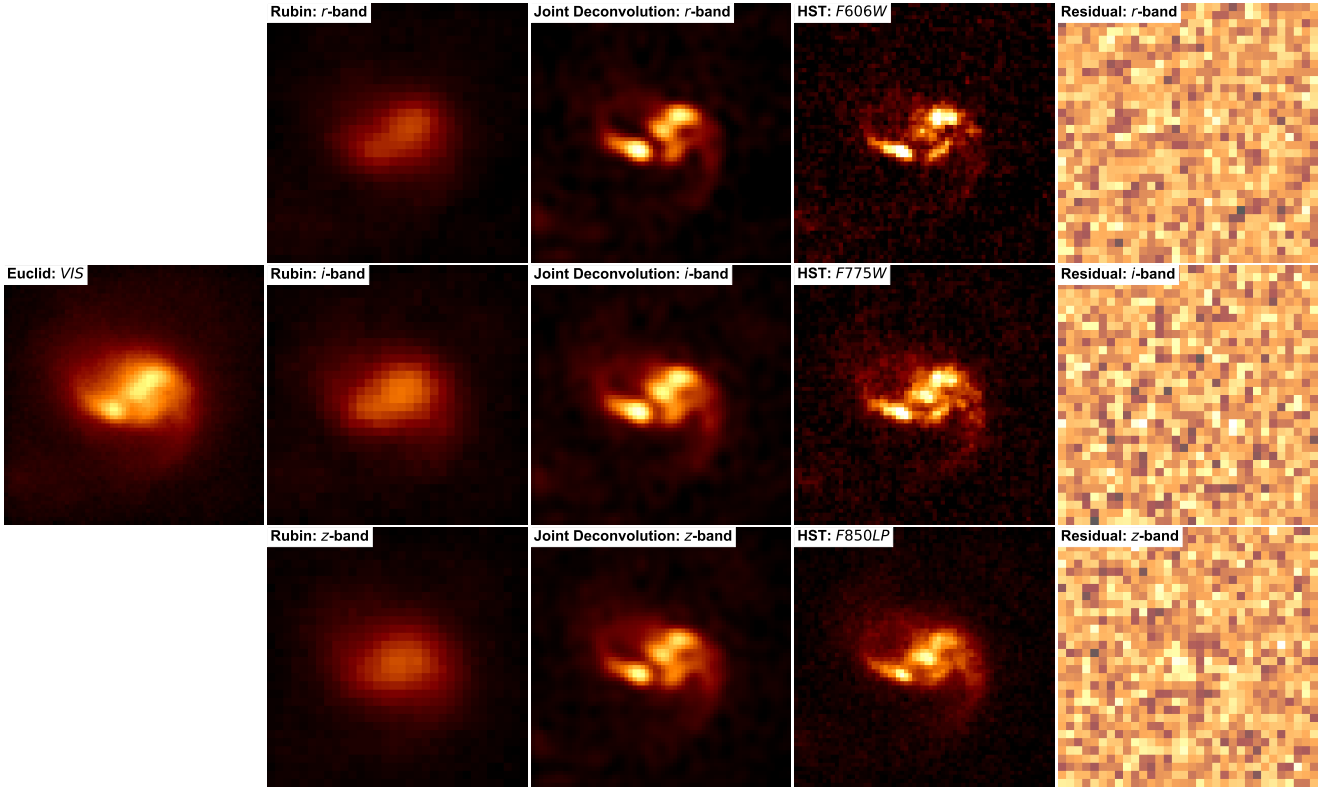
**Acknowledgements.** This work was funded by the Swiss National Science Foundation (SNSF) under the Sinergia grant number CRSII5\_198674. This work was supported by the TITAN ERA Chair project (contract no. 101086741) within the Horizon Europe Framework Program of the European Commission, and the Agence Nationale de la Recherche (ANR-22-CE31-0014-01 TOSCA).

## References

- Abolfathi, B., Alonso, D., Armstrong, R., et al. 2021, *The Astrophysical Journal Supplement Series*, 253, 31
- Agustsson, E. & Timofte, R. 2017, in *2017 IEEE Conference on Computer Vision and Pattern Recognition Workshops (CVPRW)*, 1122–1131
- Akhaury, U., Jablonka, P., Starck, J.-L., & Courbin, F. 2024, Ground-based image deconvolution with Swin Transformer UNet
- Akhaury, U., Starck, J.-L., Jablonka, P., Courbin, F., & Michalewicz, K. 2022, *Frontiers in Astronomy and Space Sciences*, 9
- Beck, A. & Teboulle, M. 2009, *SIAM Journal on Imaging Sciences*, 2, 183
- Bigdeli, S. A., Jin, M., Favaro, P., & Zwicker, M. 2017, in *Proceedings of the 31st International Conference on Neural Information Processing Systems, NIPS'17 (USA: Curran Associates Inc.)*, 763–772
- Boyd, S., Parikh, N., Chu, E., Peleato, B., & Eckstein, J. 2010, *Machine Learning*, 3, 1
- Cantale, N., Courbin, F., Tewes, M., Jablonka, P., & Meylan, G. 2016, *A&A*, 589, A81
- Chen, Y. & Pock, T. 2017, *IEEE Transactions on Pattern Analysis and Machine Intelligence*, 39, 1256
- Donath, A., Siemiginowska, A., Kashyap, V., Dyk, D. V., & Burke, D. 2023, *Bulletin of the AAS*, 55, <https://baas.aas.org/pub/2023n4i103p55>
- Euclid Collaboration, Scaramella, R., Amiaux, J., et al. 2022, *A&A*, 662, A112
- Fan, C.-M., Liu, T.-J., & Liu, K.-H. 2022, in *2022 IEEE International Symposium on Circuits and Systems (ISCAS) (IEEE)*
- Gupta, H., Jin, K. H., Nguyen, H. Q., McCann, M. T., & Unser, M. 2018, *IEEE Transactions on Medical Imaging*, 37, 1440
- H. Chan, S., Wang, X., & A. Elgendy, O. 2016, *IEEE Transactions on Computational Imaging*, PP
- He, K., Zhang, X., Ren, S., & Sun, J. 2016, in *2016 IEEE Conference on Computer Vision and Pattern Recognition (CVPR)*, 770–778
- Ingaramo, M., York, A. G., Hoogendoorn, E., et al. 2014, *ChemPhysChem*, 15, 794
- Joseph, R., Melchior, P., & Moolekamp, F. 2021, Joint survey processing: combined resampling and convolution for galaxy modelling and deblending
- Liaudat, T., Starck, J.-L., Kilbinger, M., & Frugier, P.-A. 2022, Rethinking data-driven point spread function modeling with a differentiable optical model
- Lim, B., Son, S., Kim, H., Nah, S., & Lee, K. M. 2017, in *2017 IEEE Conference on Computer Vision and Pattern Recognition Workshops (CVPRW)*, 1132–1140
- Lucy, L. B. 1974, *AJ*, 79, 745

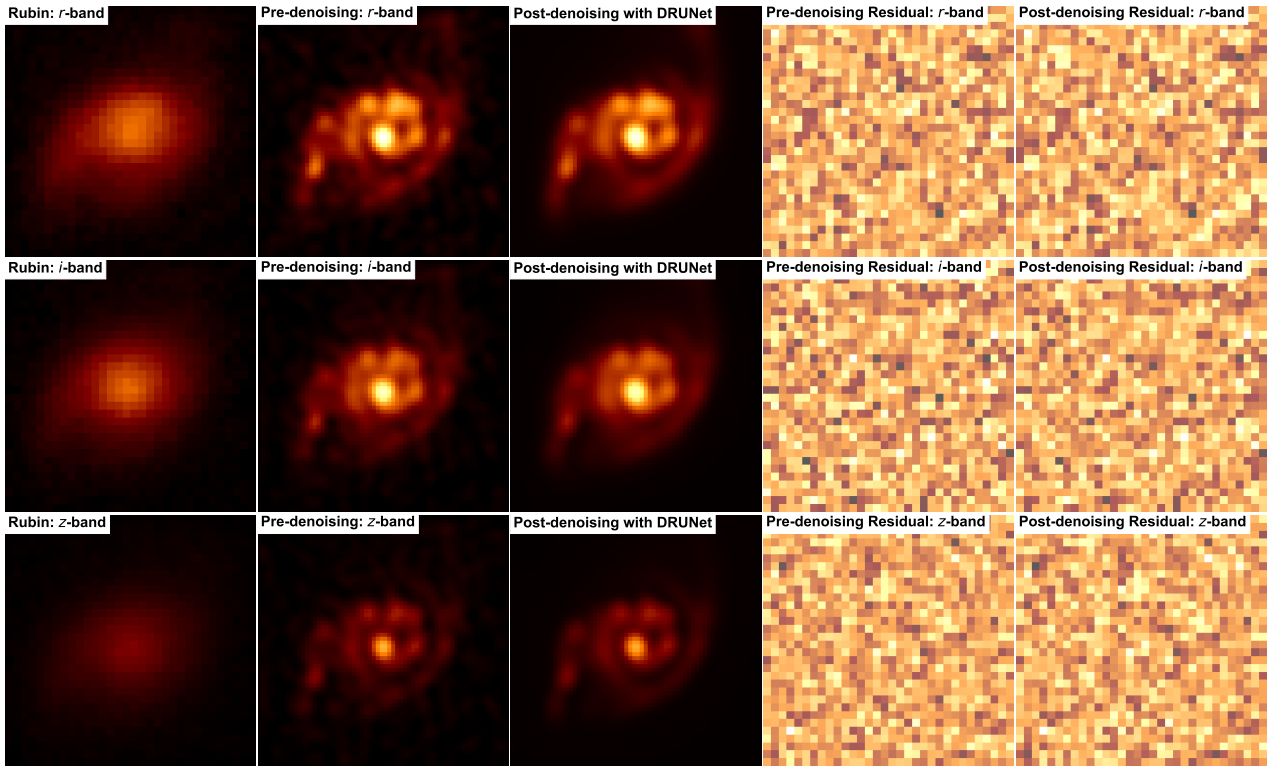


(a)

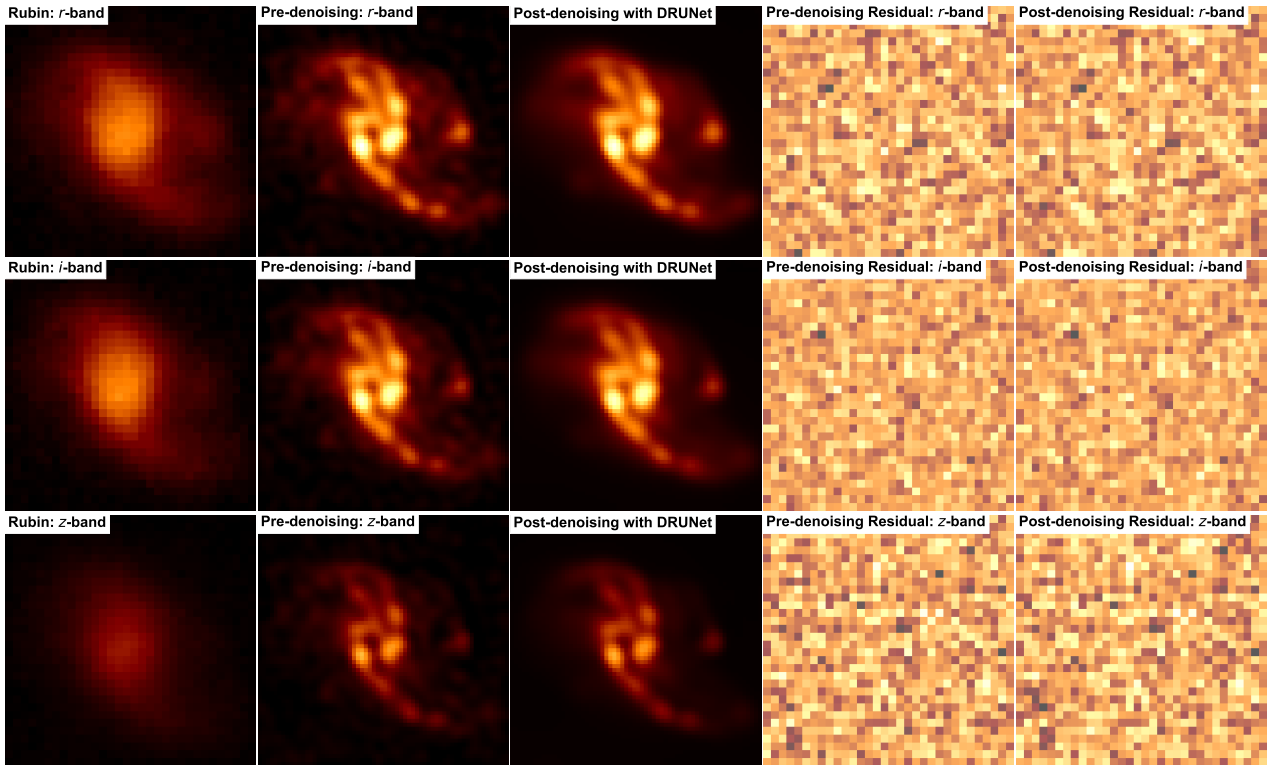


(b)

Fig. 7: Two deconvolved outputs, illustrating the successful recovery of features completely lost in the *Vera C. Rubin* simulations. Additionally, the outputs seem to capture the variations when transitioning from one band to another. The first column displays the *Euclid VIS* image, followed by *Vera C. Rubin* simulations in the *r*, *i*, and *z* bands in the second column. The deconvolved outputs for the three bands are shown in the third column. The fourth column shows corresponding ground-truth HST images, followed by residuals in the fifth column, which are defined as follows: residual = noisy *Vera C. Rubin* image – PSF \* deconvolved image.



(a)



(b)

Fig. 8: Two denoised outputs from DRUNet, demonstrating its ability to effectively remove noise from the background while preserving the structure of the central galaxy. The first column displays *Vera C. Rubin* simulations in the  $r$ ,  $i$ , and  $z$  bands. The second column shows the corresponding pre-denoised outputs. The third column displays the corresponding post-denoised outputs, followed by the residuals in the fourth and fifth columns, respectively.

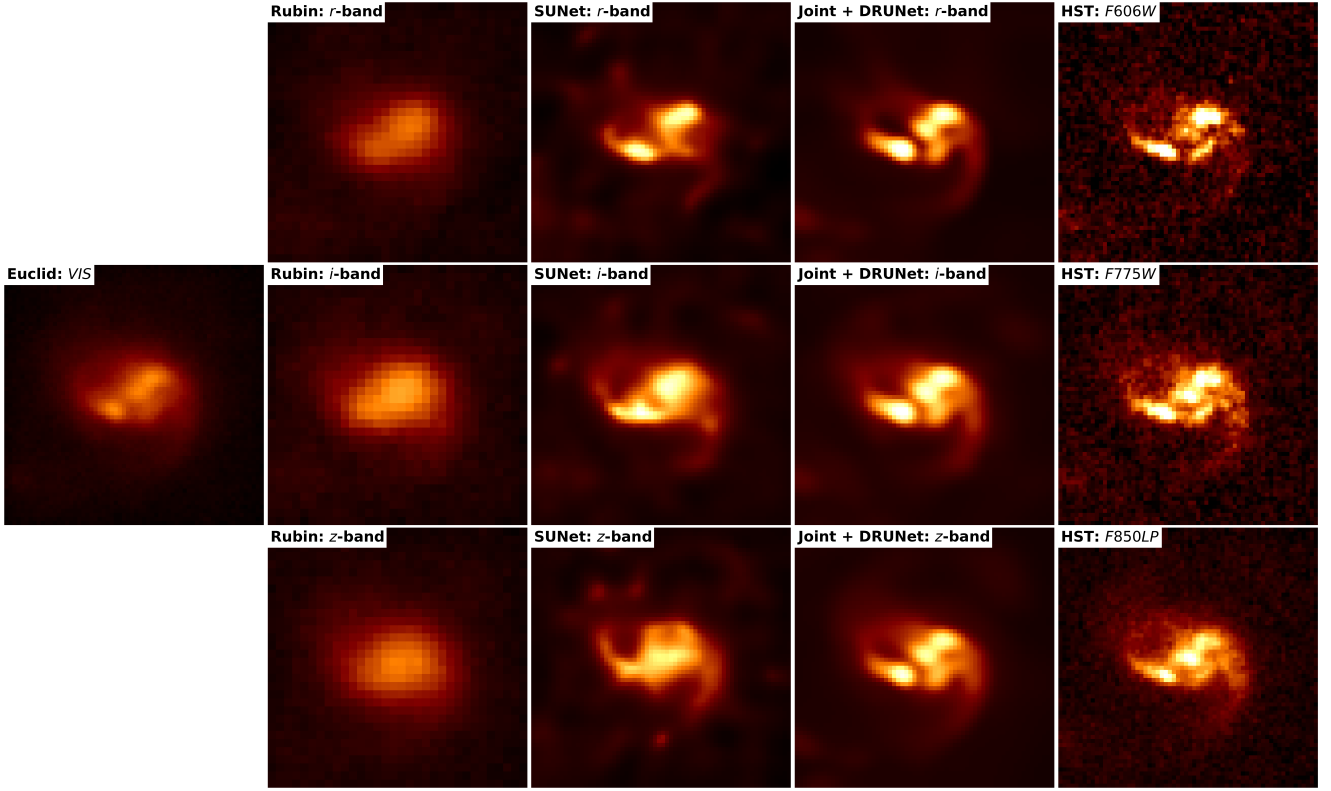


Fig. 9: The galaxy in Figure 7b deconvolved using two different approaches, illustrating that joint deconvolution outperforms independent deconvolution of individual photometric bands. The joint method allows us to leverage the correlation between the different bands and the space-based image, thus improving the final output. The first column displays the *Euclid* *VIS* image, followed by *Vera C. Rubin* simulations in the *r*, *i*, and *z* bands in the second column. The independently deconvolved SUNet outputs for the three bands are shown in the third column. The fourth column shows the corresponding joint deconvolution outputs followed by denoising with DRUNet. The ground-truth HST images are shown in the fifth column.

26, 1004  
 Magain, P., Courbin, F., & Sohy, S. 1998, *The Astrophysical Journal*, 494, 472  
 Meinhardt, T., Moller, M., Hazirbas, C., & Cremers, D. 2017, in *Proceedings of the IEEE International Conference on Computer Vision*, 1781–1790  
 Michalewicz, K., Millon, M., Dux, F., & Courbin, F. 2023, *Journal of Open Source Software*, 8, 5340  
 Nammour, F., Akhaury, U., Girard, J. N., et al. 2022, *A&A*, 663, A69  
 Ramzi, Z., Michalewicz, K., Starck, J.-L., Moreau, T., & Ciuciu, P. 2023, *Journal of Mathematical Imaging and Vision*, 65, 240  
 Retzlaff, J., Rosati, P., Dickinson, M., et al. 2010, *A&A*, 511, A50  
 Richardson, W. H. 1972, *Journal of the Optical Society of America* (1917-1983), 62, 55  
 Ronneberger, O., Fischer, P., & Brox, T. 2015, *CoRR*, abs/1505.04597 [arXiv:1505.04597]  
 Skilling, J. & Bryan, R. K. 1984, *MNRAS*, 211, 111  
 Sreehari, S., Venkatakrishnan, S., Wohlberg, B., et al. 2016, *IEEE Transactions on Computational Imaging*, 2, 408  
 Starck, J.-L., Murtagh, F., & Bertero, M. 2015, *Starlet Transform in Astronomical Data Processing*, ed. O. Scherzer (New York, NY: Springer New York), 2053–2098  
 Sureau, F., Lechat, A., & Starck, J.-L. 2020, *A&A*, 641, A67  
 Tikhonov, A. N. & Arsenin, V. Y. 1977, *Solutions of ill-posed problems* (Washington, D.C.: John Wiley & Sons, New York: V. H. Winston & Sons), xiii+258, translated from the Russian, Preface by translation editor Fritz John, *Scripta Series in Mathematics*  
 van der Walt, S., Schönberger, J. L., Nunez-Iglesias, J., et al. 2014, *CoRR*, abs/1407.6245 [1407.6245]  
 Venkatakrishnan, S. V., Bouman, C. A., & Wohlberg, B. 2013, 2013 *IEEE Global Conference on Signal and Information Processing*, 945  
 VenkateshG, M., Naresh, Y. G., Little, S., & O'Connor, N. E. 2018, in *OR 2.0/CARE/CLIP/ISIC@MICCAI*  
 Zhang, K., Li, Y., Zuo, W., et al. 2022, *IEEE Transactions on Pattern Analysis and Machine Intelligence*, 44, 6360  
 Zhang, K., Zuo, W., & Zhang, L. 2018a, *IEEE Transactions on Image Processing*, 27, 4608

Zhang, Z., Liu, Q., & Wang, Y. 2018b, *IEEE Geoscience and Remote Sensing Letters*, 15, 749  
 Željko Ivezić, Kahn, S. M., Tyson, J. A., et al. 2019, *The Astrophysical Journal*, 873, 111

## Appendix A: Generalization to objects with non-flat spectral energy distribution (SED)

To assess the impact of information transfer across different bands for objects with a non-flat spectral energy distribution (SED), we conducted an experiment where we successively replaced the *Rubin* bands with pure noise, ensuring that no galaxy signal was present. We then analyzed how features from the high-resolution *Euclid* image propagated into the deconvolved *Rubin* bands. The outputs are shown in Figure A.1.

Our results confirm that reconstructed features appear only in bands where the original galaxy signal is present. This demonstrates that the algorithm does not artificially imprint *Euclid* information onto *Rubin* bands lacking real data. In cases where a structure is visible in the *Euclid* image but absent from one or more *Rubin* bands, the problem becomes degenerate: the feature could either be entirely attributed to a single band or distributed across multiple bands. However, our findings indicate that the outputs are directly influenced by the input data in each band rather than being dictated solely by the high-resolution *Euclid* image. Our results demonstrate that the joint deconvolution method effectively utilises the available signal in each band while respecting the constraints imposed by the data. This also confirms that the method would work for objects with non-flat SEDs, where signal may be present in only one band but absent in others, ensuring that features are accurately transferred according to their actual distribution across the bands.

As mentioned in Section 4, we found that the algorithm converges within 200 iterations when the signal is available in all three bands. When one band is replaced with a noisemap, as shown in Figure 1a, convergence requires approximately 1000 iterations. Replacing a second band with a noisemap, as seen in Figure 1b, further increases the iteration count to around 5000. This demonstrates that incorporating more data across different bands significantly accelerates the convergence of the loss functions as the algorithm can benefit by capturing the correlations between these bands.

## Appendix B: Plug-and-Play ADMM

Plug-and-Play Alternating Direction Method of Multipliers (PnP ADMM) has emerged as a powerful framework for solving inverse problems by combining iterative optimization techniques with deep learning-based priors. Originally developed for convex optimization problems with linear equality constraints (Boyd et al. 2010), ADMM decomposes the minimization process into sequential sub-problems, typically involving a data fidelity term and a regularization term, followed by an update of the dual variable. Previous works (Venkatakrishnan et al. 2013; Sreehari et al. 2016; H. Chan et al. 2016) have interpreted these sub-steps as an inversion step followed by a denoising step, coupled via the augmented Lagrangian term and the dual variable. The ADMM PnP approach extends this idea by replacing the proximal operator related to the prior with a deep neural network (DNN) trained as a denoiser (Meinhardt et al. 2017; Bigdeli et al. 2017; Gupta et al. 2018;ureau et al. 2020), allowing for greater flexibility in handling complex image priors. Compared to direct deep-learning-based inverse models, PnP ADMM offers several advantages: (1) it decouples the inversion step from the DNN, enabling the inclusion of additional convex constraints that can be efficiently handled via optimization, (2) it reduces the cost of learning by focusing solely on training a denoiser rather than multiple networks, as seen in unfolding approaches, and (3) by iterating between denoising and inversion, it ensures that the

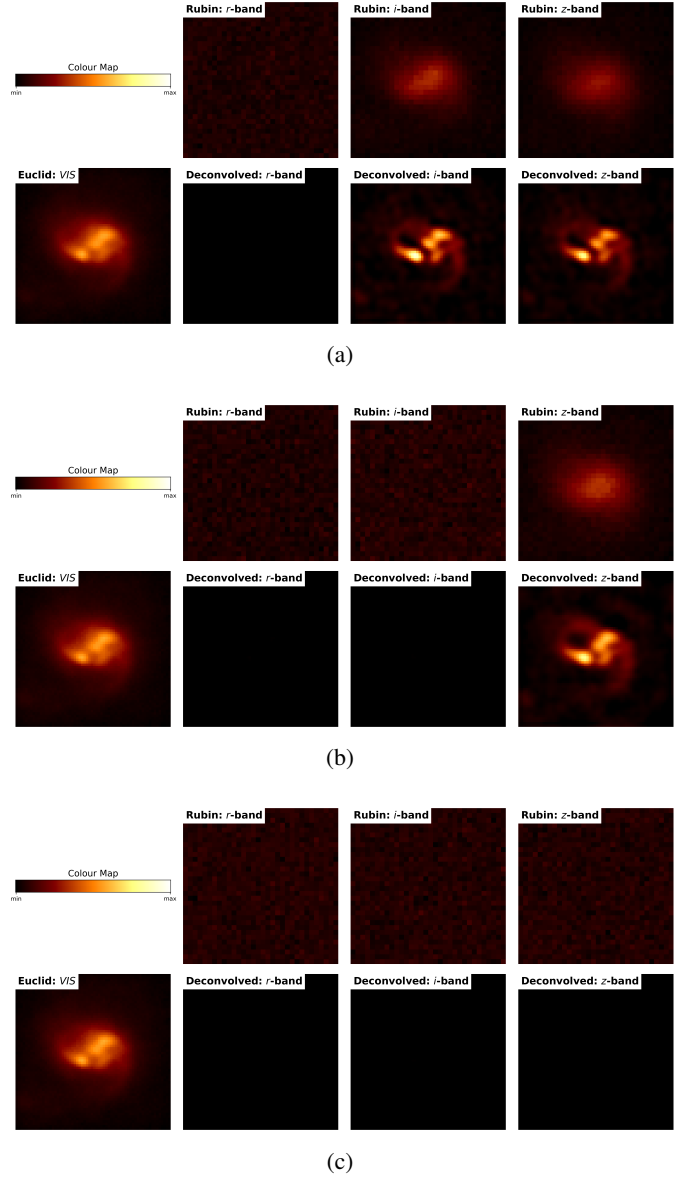


Fig. A.1: The galaxy from Figure 7b, with each band being successively replaced by a random noise map, as shown when progressing from subfigure 1a to 1c. Reconstructed features appear only in bands where the original galaxy signal is present.

network output remains consistent with the observed data. In this work, we integrate the PnP ADMM framework from Bureau et al. (2020) with the DRUNet denoiser from Zhang et al. (2022). Specifically, we employ DRUNet in the proximal update step of the PnP framework to enhance the denoising performance.

### Appendix B.1: The proposed solution

Considering the forward model described in Section 2.1, we defined the following loss functions, akin to equations 6-8, but incorporating an additional augmented Lagrangian term with the dual variable. These functions were then minimized using the algorithm outlined in Section B.2.

---

**Algorithm 1** Plug-and-Play ADMM algorithm to deconvolve a galaxy image, inspired by Sureau et al. (2020)
 

---

```

1: Initialize: Set  $\rho_0 = 1, \rho_{max} = 10, \eta = 0.5, \gamma = 1.4, \Delta_0 = 0, \mathbf{x}^{(0)} = \mathbf{y}, \mathbf{z}^{(0)} = \mathbf{x}^{(0)}, \boldsymbol{\mu}^{(0)} = 0, \epsilon$ 
2: for  $k = 0$  to  $N_{iterations}$  do {Main Loop}
3:   Deconvolution sub-problem:  $\mathbf{x}^{(k+1)} = FISTA(\mathbf{y}, \mathbf{x}^{(k)}, \mathbf{z}^{(k)}, \boldsymbol{\mu}^{(k)}, \rho_k)$  (Beck & Teboulle 2009)
4:   Denoising sub-problem:  $\mathbf{z}^{(k+1)} = N_\theta(\mathbf{x}^{(k+1)} + \boldsymbol{\mu}^{(k)})$  ( $N_\theta$  = DRUNet denoiser)
5:   Lagrange multiplier update:  $\boldsymbol{\mu}^{(k+1)} = \boldsymbol{\mu}^{(k)} + (\mathbf{x}^{(k+1)} - \mathbf{z}^{(k+1)})$ 
6:    $\Delta_{k+1} = \frac{1}{\sqrt{n}} (\|\mathbf{x}^{(k+1)} - \mathbf{x}^{(k)}\|_2 + \|\mathbf{z}^{(k+1)} - \mathbf{z}^{(k)}\|_2 + \|\boldsymbol{\mu}^{(k+1)} - \boldsymbol{\mu}^{(k)}\|_2)$ 
7:   if  $\Delta_{k+1} \geq \eta \Delta_k$  and  $\rho_{k+1} \leq \rho_{max}$  then
8:      $\rho_{k+1} = \gamma \rho_k$ 
9:   else
10:     $\rho_{k+1} = \rho_k$ 
11:   end if
12: end for
13: return  $\{\mathbf{x}^{(k+1)}\}$ 
    
```

---

$$L_r(\mathbf{x}_r) = \frac{1}{2} \left\| \frac{\mathbf{h}_r * \mathbf{x}_r - \mathbf{y}_r}{\sigma_r} \right\|_F^2 + \frac{\rho}{2} \|\mathbf{x}_r - \mathbf{z}_r + \boldsymbol{\mu}_r\|_F^2 + \lambda_r \mathbf{K} \quad (\text{B.1})$$

$$L_i(\mathbf{x}_i) = \frac{1}{2} \left\| \frac{\mathbf{h}_i * \mathbf{x}_i - \mathbf{y}_i}{\sigma_i} \right\|_F^2 + \frac{\rho}{2} \|\mathbf{x}_i - \mathbf{z}_i + \boldsymbol{\mu}_i\|_F^2 + \lambda_i \mathbf{K} \quad (\text{B.2})$$

$$L_z(\mathbf{x}_z) = \frac{1}{2} \left\| \frac{\mathbf{h}_z * \mathbf{x}_z - \mathbf{y}_z}{\sigma_z} \right\|_F^2 + \frac{\rho}{2} \|\mathbf{x}_z - \mathbf{z}_z + \boldsymbol{\mu}_z\|_F^2 + \lambda_z \mathbf{K} \quad (\text{B.3})$$

$$\text{where } \mathbf{K} = \left\| \frac{\mathbf{h}_{euc} * \sum_{c \in \{r,i,z\}} \alpha_c \mathbf{x}_c - \mathbf{y}_{euc}}{\sigma_{euc}} \right\|_F^2 \quad (\text{B.4})$$

As before, the first terms in equations B.1-B.3 represent the data fidelity terms for each respective band, with  $\sigma_r, \sigma_i, \sigma_z$  being the corresponding noisemaps. The second terms represent the augmented Lagrangian, incorporating the dual variable  $\mathbf{z}$  to split the problem into two sub-problems: an inversion/deconvolution step followed by a denoising step. The third terms, as explained in Section 2.2, are the constraining terms that enforce the condition that the sum of images in the *Rubin*  $r$ -,  $i$ -, and  $z$ -band images equals the *Euclid* *VIS*-band images. For the ADMM update, the parameter  $\rho$  was manually tuned based on the approach from Sureau et al. (2020) to strike a balance between quickly stabilizing the algorithm (with a higher  $\rho$ ) and prioritizing the minimization of the data fidelity term in the early iterations (with a lower  $\rho$ ). The values of all other hyperparameters have been previously described in Sections 2.2 and 2.3.

#### Appendix B.2: The algorithm

The PnP ADMM algorithm inspired by Sureau et al. (2020) is summarized in Table 1. The first step consists of solving the loss functions B.1-B.3 alternatively at iteration  $k$  using the accelerated iterative convex algorithm FISTA (Beck & Teboulle 2009). In the second step, the DRUNet denoiser functions as a projector in the proximal update step, as described earlier. The final step regulates the augmented Lagrangian parameter, ensuring its increase when the optimization parameters exhibit insufficient change.

#### Appendix B.3: Results

The algorithm simultaneously processed the noisy simulations from the three *Vera C. Rubin* bands and the *Euclid* *VIS*-band, along with their respective PSFs. These noisy images served as initializations or first guesses. The algorithm was run for 200 iterations, with convergence typically observed within 150-200 iterations for all images in our dataset. Figure B.1 shows the convergence plot of the loss function for the deconvolved output in Figure 2a.

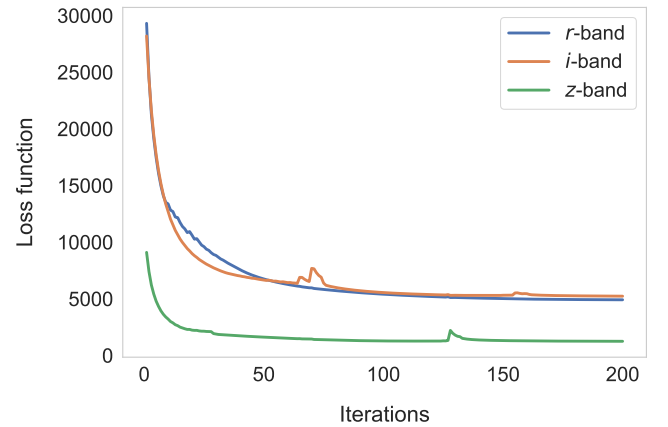
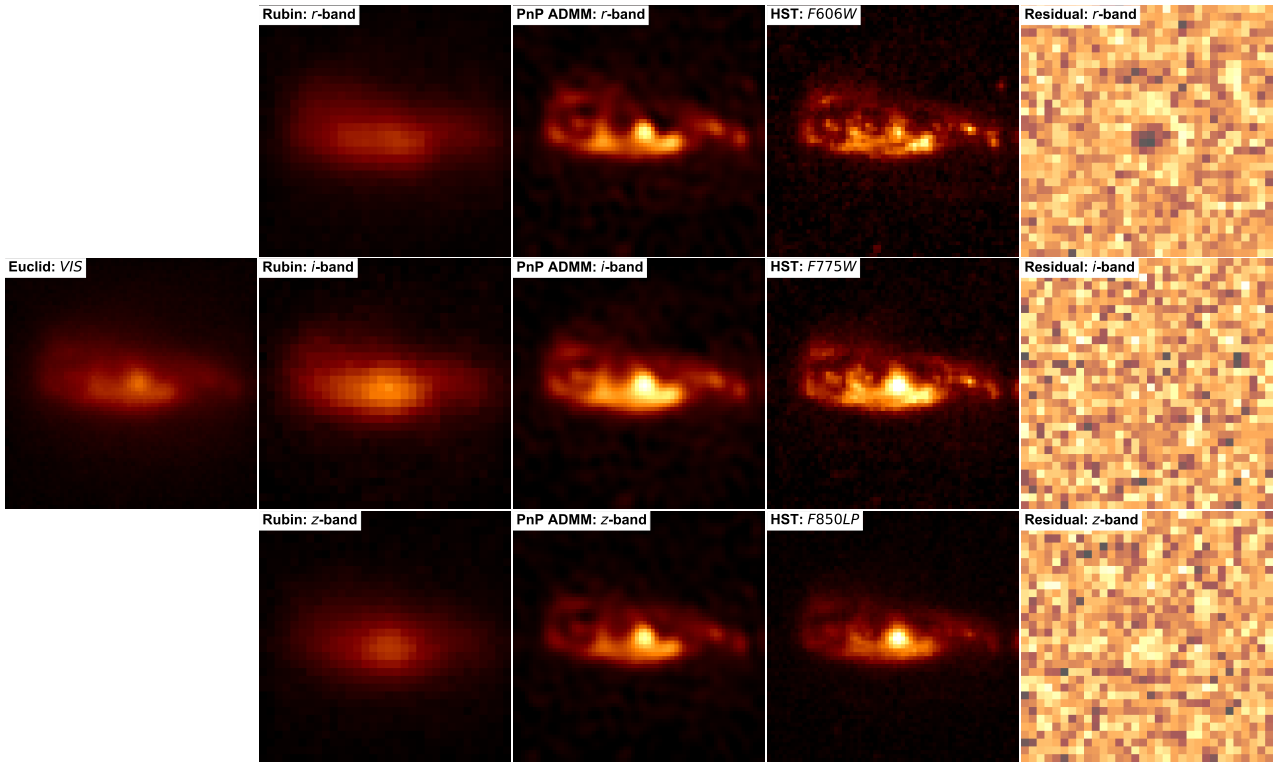
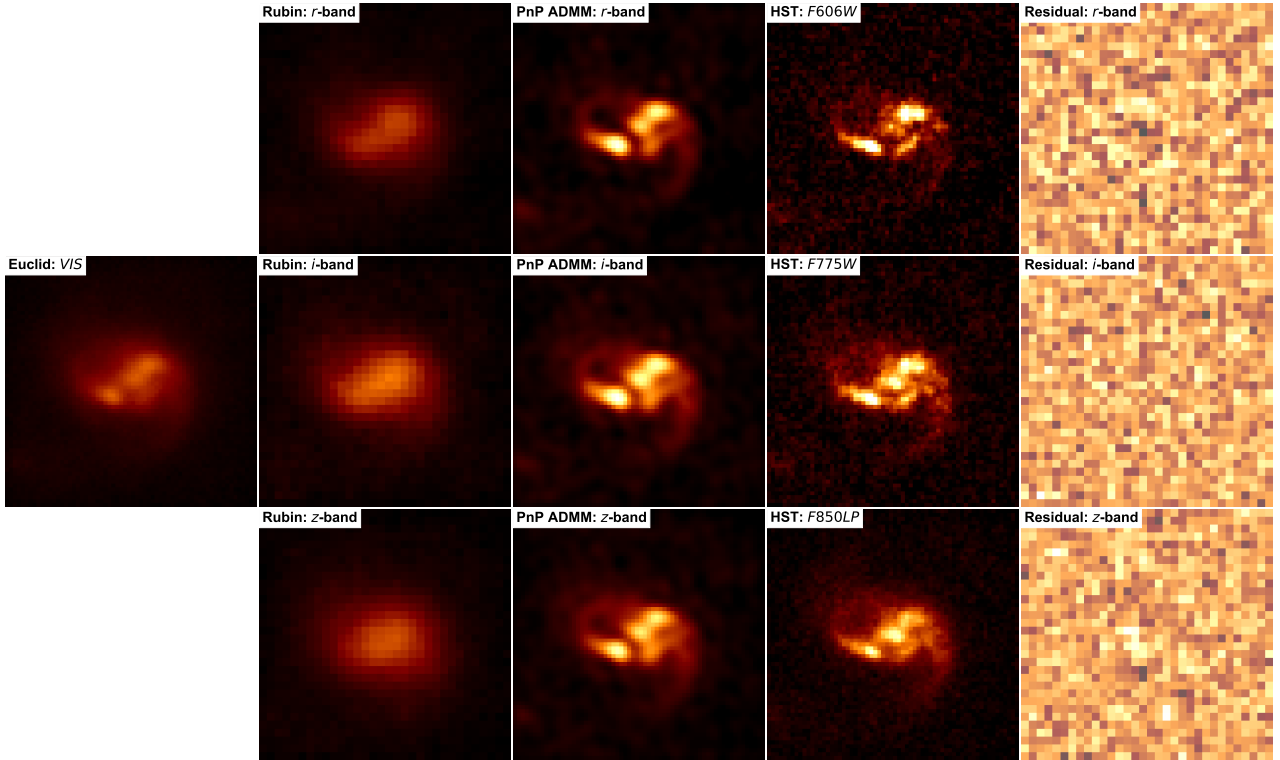


Fig. B.1: The loss function for the galaxy shown in Figure 2a. Convergence is achieved at around 200 iterations when the relative change in loss value  $< 10^{-3}$  and the curve is flat.

Figure B.2 presents the same two examples of deconvolved images as shown in Figure 7. Qualitatively, the outputs for the two methods closely resemble each other. Compared to the original algorithm, there is a slight reduction in NMSE by approximately 0.26%. However, due to the additional computational steps involved in the iterative process and the proximal denoising step, PnP ADMM takes approximately 50 times longer to run than the original algorithm. This is consistent with the findings of Sureau et al. (2020). Hence, this significant increase in computational time makes it less practical for use on large datasets.



(a)



(b)

Fig. B.2: Outputs of the PnP ADMM algorithm for the two galaxies shown in Figure 7, closely matching the results presented in the same figure. The first column displays the *Euclid VIS* image, followed by *Vera C. Rubin* simulations in the *r*, *i*, and *z* bands in the second column. The deconvolved outputs for the three bands are shown in the third column. The fourth column shows corresponding ground-truth HST images, followed by residuals in the fifth column.